Incorporating Goodness-of-fit Metrics to Improve Synchrophasor-based Fault Location

Matin Rahmatian *Student Member, IEEE*, Yu Christine Chen *Member, IEEE*,
William G. Dunford *Senior Member, IEEE*, and Farnoosh Rahmatian *Fellow, IEEE*

***Abstract*—This paper proposes to incorporate goodness-of-fit (GoF) metrics as outputs—in addition to the synchronized phasor (or synchrophasor)—from a phasor measurement unit (PMU) to assess the performance quality of synchrophasor-based real-time applications, with specific focus on the accuracy of fault location along a transmission line. Typically, a PMU outputs quantities that describe the phasor-of-best-fit of a time-domain voltage or current signal. While a phasor accurately represents the actual measured signal in sinusoidal steady state, this may not be the case during electrical transients that occur immediately after sudden events, such as a fault. Unaware of this, the real-time application may not locate the fault accurately. By quantifying the accuracy of the phasor as compared with the actual time-domain signal to which the phasor is fit, GoF metrics help to assess the credibility of fault-location results. This hypothesis is verified via extensive case studies, and GoF-based criteria for sufficiently accurate fault-location results are uncovered.**

***Index Terms*—Fault location, goodness of fit, phasor measurement units, synchrophasor,**

I. Introduction

THE transmission grid transfers large amounts of electric power from generators to load centres via a complex network of transmission lines. From time to time, these lines experience faults caused by various events, such as storms, lightning, and insulation aging and breakdown [1]. In order to ensure system-wide power availability and quality, maintenance crews must swiftly repair damages and restore the faulted line. Vital to accomplishing these tasks are real-time tools that accurately pinpoint the fault location along the line of interest in a timely manner. Existing methods can be broadly categorized into (i) single-end methods and (ii) double- or multi-end methods. Single-end methods (see, e.g., [2], [3]) utilize measurements obtained from only one end of the faulted line and do not need data from remote buses, but fault-location results may not be accurate. On the other hand, methods that utilize measurements from both ends (or multiple ends in case of multi-terminal lines) of the faulted line are generally more accurate [4], [5]. Nevertheless, unsynchronized measurements obtained from remote buses may cause fault-location errors, which is a shortcoming that has been identified in the literature [6], [7]. An enabling technology that can address this challenge is the phasor measurement unit (PMU), which provides synchronized-phasor (or synchrophasor) measurements [8].

The PMU fits a phasor to a time-domain signal collected by a current or voltage transformer, and further reports the phasor amplitude, phase angle, frequency, and rate of change of frequency [9]. These quantities are all synchronized and tagged with an accurate coordinated universal time stamp by using, e.g., the reference time acquired through global positioning system receivers [9]. Thereafter, a wide-area communication network enables synchrophasor measurements to be transmitted from various PMUs to phasor data collectors (PDCs) and then a central location [10]. These measurements may be used by real-time application deployed at the level of a single PMU, a local PDC, or a central decision maker [11].

Recognizing the potential for synchrophasors to reduce fault-location errors arising from unsynchronized measurements, numerous approaches have been proposed to take advantage of them [12]–[14]. However, these do not address the impact of phasor measurement errors on the resulting fault-location accuracy or credibility. A typical metric to quantify errors in the PMU output is the total vector error (TVE), which measures the difference between the information from a PMU that describes a phasor and the true phasor itself [9], [15]. Such a metric is relevant only if the actual voltage and current signal of interest is in sinusoidal steady state. However, immediately following sudden events, such as fault initiation and clearance, voltages and currents experience electrical transients that render the sinusoidal steady-state assumption held by the TVE metric invalid. To address this shortcoming, the goodness-of-fit (GoF) metric measures the difference between the time-domain waveform reconstructed from the phasor measurement and the actual voltage or current signal [16]. By explicitly comparing the *time-domain* signals, the GoF metric is applicable under both sinusoidal steady-state and electrically transient operating conditions. This is particularly relevant for real-time reliability-critical applications—such as fault location—that use synchrophasors obtained while the system experiences electrical transients. In this paper, to transition synchrophasor-based fault location to a practical solution for industry use, we focus on GoF metrics to help quantify synchrophasor accuracy during fault conditions and, in turn, to assess the confidence level of the ensuing fault-location results.

Given that double-end fault-location methods are easily implementable with the modern communication infrastructure in today's power system, we focus on such a method similar to that described in [12] and extend it to locate (possibly

M. Rahmatian, Y. C. Chen, and W. G. Dunford are with the Department of Electrical and Computer Engineering at The University of British Columbia, Vancouver, BC, Canada. E-mail: {mrahmatian, chen, wgd}@ece.ubc.ca.

F. Rahmatian is with NuGrid Power Corporation, Vancouver, BC, Canada. E-mail: frahmatian@nugridpower.com.

M. Rahmatian and Y. C. Chen gratefully acknowledge the support of the Natural Sciences and Engineering Research Council of Canada (NSERC), funding reference numbers RGPIN-2016-04271 and 514710-17.

unsymmetric) faults along three-phase transmission lines using synchrophasors. Next, via a numerical example, we highlight that the accuracy of fault-location results depends on how well voltage or current waveforms can be approximated as phasors. In order to quantify the mismatch between actual time-domain waveforms and their phasor representations during electrical transients, we use the GoF metric described in [16], as well as a variant of it. With the GoF metrics in hand, we perform numerous simulations for various fault conditions and locations along a transmission line to investigate the relationship between the accuracy of synchrophasor-based fault-location results and the GoF values for corresponding phasors. Through extensive numerical case studies, we observe that synchrophasors with GoF values above certain thresholds provide sufficient confidence levels in the accuracy of fault-location results. Thus, we recommend to include GoF metrics as additional prescribed quantities for PMUs to transmit to the fault-location application. Such a modification may also help to assess the accuracy of results from other synchrophasor-based applications that require a high level of confidence (as is often the case in production-grade real-time applications in the electric power industry).

The remainder of the paper is organized as follows. In Section II, we extend the method in [12] to locate a (possibly unsymmetric) fault along a three-phase line and to identify the faulted phases. Then, by comparing simulation cases for which this method returns accurate versus inaccurate fault-location results, we motivate the need for a GoF metric. This metric and a variant are defined with numerical illustration of their properties in Section III. In Section IV, the advantages of incorporating GoF metrics into PMUs are demonstrated through numerical case studies. Finally, concluding remarks and directions for future work are offered in Section V.

II. Background

Following the release of [9], synchrophasor algorithms have been further investigated with the aim of improving the basic model in [9] to meet the static and dynamic performance requirements assigned in industry standards (see, e.g., [17]–[19]). Synchrophasors obtained from PMUs can be categorized into two performance classes: measurement (M-class) and protection (P-class) [15]. Since the focus of this paper is on a specific application of PMUs for system protection, we elect to use the basic P-class PMU model proposed in Annex C of [9], from which measurements are extracted. However, we note that the choice of a more detailed PMU model would not affect our analysis or results significantly. In this section, PMU measurements are used to estimate steady-state transmission-line impedances and to locate unsymmetric faults. Through the fault-location application, we motivate the need to incorporate GoF metrics for PMU measurements.

A. Measurement-based Estimation of Line Impedance

Steady-state transmission-line impedance values are prone to variations of up to 40% under various ambient and loading conditions [20]. In order to ensure accurate fault-location results, the pre-fault steady-state line impedance for each phase must be updated periodically to match evolving operating conditions. Inspired by the parameter-free method proposed in [12], in which measurements in the pre-fault period are used instead of relying on *a priori* knowledge of line parameters, below we estimate steady-state lumped line parameters assuming three-phase balanced impedances. With reference to Fig. 1a, we assume that P-class PMUs are installed at buses m and n, which are connected via the transmission line of interest, and per-phase bus-voltage and current-flow measurements are available.

Suppose PMU phasor measurements are reported at intervals of Δt, i.e., at times $t_k = k\Delta t$, $k = 1, 2, \ldots$ Denote measured voltages (as phasors) at bus m and time t_k for phases a, b, and c as $V_m^a[k]$, $V_m^b[k]$, and $V_m^c[k]$, respectively. Further denote the measured currents (as phasors) through line (m, n) (assume positive flow from bus m to n measured at bus m) at time t_k in phases a, b, and c as $I_{(m,n)}^a[k]$, $I_{(m,n)}^b[k]$, and $I_{(m,n)}^c[k]$, respectively. Collect per-phase voltage measurements at bus m into $V_m[k] = [V_m^a[k], V_m^b[k], V_m^c[k]]^{\mathrm{T}}$; also collect per-phase measurements of currents in line (m, n) into $I_{(m,n)}[k] = [I_{(m,n)}^a[k], I_{(m,n)}^b[k], I_{(m,n)}^c[k]]^{\mathrm{T}}$. In symmetrical components, the voltage at bus m is defined as $V_m^{\mathrm{s}}[k] := T^{-1}V_m[k]$, where T is the so-called *symmetrical components transformation matrix* [21]. Similarly, for currents through line (m, n), $I_{(m,n)}^{\mathrm{s}}[k] = T^{-1}I_{(m,n)}[k]$. With these definitions in place, consider a three-phase line with balanced impedances, for which the circuit in symmetrical components is decoupled into three independent impedance networks, i.e., [21]

$$V_m^{\mathrm{s}}[k] - V_n^{\mathrm{s}}[k] = \mathrm{diag}(Z_{(m,n)}^{\mathrm{s}})I_{(m,n)}^{\mathrm{s}}[k], \tag{1}$$

where the vector $Z_{(m,n)}^{\mathrm{s}}$ contains the positive-, negative-, and zero-sequence network impedances, and $\mathrm{diag}(Z_{(m,n)}^{\mathrm{s}})$ denotes the diagonal matrix formed with diagonal entries composed of entries of $Z_{(m,n)}^{\mathrm{s}}[k]$. Then, using per-phase voltage and current measurements obtained at time t_k, we can compute[1]

$$\begin{aligned} Z_{(m,n)}^{\mathrm{s}}[k] &= \mathrm{diag}(I_{(m,n)}^{\mathrm{s}}[k])^{-1}(V_m^{\mathrm{s}}[k] - V_n^{\mathrm{s}}[k]) \\ &= \mathrm{diag}(T^{-1}I_{(m,n)}[k])^{-1}T^{-1}(V_m[k] - V_n[k]), \end{aligned} \tag{2}$$

where the second equality above results by immediate application of the symmetrical components transformation. From (2), we can straightforwardly obtain an up-to-date estimate of the abc-frame three-phase impedance matrix as

$$Z_{(m,n)}[k] = T\mathrm{diag}(Z_{(m,n)}^{\mathrm{s}}[k])T^{-1}. \tag{3}$$

Since we consider the case of balanced impedances, the diagonal entries of $Z_{(m,n)}[k]$ (representing self impedances) have the same value, and the off-diagonal entries (representing mutual impedances) are also equal to each other.

B. Fault Location and Faulted-phase Identification

Consider a three-phase transmission line (m, n) with total length ℓ and steady-state impedance matrix estimated as $Z_{(m,n)}$ from (3), with an unknown fault imposed, as shown in Fig. 1b. In this section, we simultaneously locate

[1]We use the fact that $\mathrm{diag}(x)y = \mathrm{diag}(y)x$, where x and y are vectors of appropriate dimension.

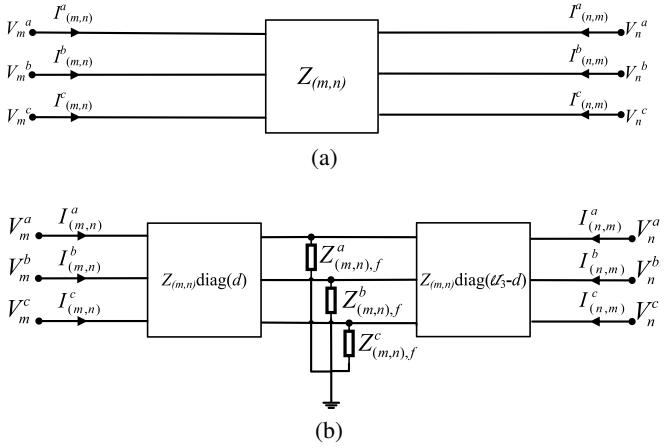

Fig. 1: Circuit model of three-phase transmission line (m, n) (see, e.g., [22]) (a) before fault, and (b) during fault. The fault location (characterized as the distance d from bus m) and the fault-to-ground impedances ($Z^a_{(m,n),f}$, $Z^b_{(m,n),f}$, and $Z^c_{(m,n),f}$) are unknown quantities. Once solved, they provide the fault location and identify the affected phases.

the fault and estimate the fault-to-ground impedance using synchrophasors obtained at buses m and n. The estimated fault location and impedance values also indicate the phases that are affected by the fault. To this end, denote the unknown distance from bus m to the fault location at time t_k as $d[k] = [d^a[k], d^b[k], d^c[k]]^{\mathrm{T}}$, where $d^a[k]$, $d^b[k]$, and $d^c[k]$ represent the distances in phases a, b, and c, respectively. Also, denote the unknown fault-to-ground impedance at time t_k as $Z_{(m,n),f}[k] = [Z^a_{(m,n),f}[k], Z^b_{(m,n),f}[k], Z^c_{(m,n),f}[k]]^{\mathrm{T}}$, where $Z^a_{(m,n),f}[k]$, $Z^b_{(m,n),f}[k]$, and $Z^c_{(m,n),f}[k]$ represent fault-to-ground impedances in phases a, b, and c, respectively. The variables $d[k]$ and $Z_{(m,n),f}[k]$ are unknowns to be solved in this problem. Based on the circuit in Fig. 1b, we can express three-phase KVL equations from bus m to n at time t_k as

$$\begin{aligned} V_m[k] - V_n[k] &= Z_{(m,n)}\left(\text{diag}(d[k])\right) I_{(m,n)}[k] \\ &\quad - Z_{(m,n)}\text{diag}(\ell\mathbb{1}_3 - d[k]) I_{(n,m)}[k] \\ &= Z_{(m,n)}\text{diag}\left(I_{(m,n)}[k] + I_{(n,m)}[k]\right) d[k] \\ &\quad - \ell Z_{(m,n)} I_{(n,m)}[k] \\ &=: A_1[k]d[k] - c[k], \end{aligned} \tag{4}$$

where $\mathbb{1}_3 = [1, 1, 1]^{\mathrm{T}}$. Similarly, we can write another KVL equation at time t_k from bus m to ground as

$$\begin{aligned} V_m[k] &= Z_{(m,n)}\text{diag}(d[k]) I_{(m,n)}[k] \\ &\quad + \text{diag}(Z_{(m,n),f}[k])(I_{(m,n)}[k] + I_{(n,m)}[k]) \\ &= Z_{(m,n)}\text{diag}(I_{(m,n)}[k]) d[k] \\ &\quad + \text{diag}(I_{(m,n)}[k] + I_{(n,m)}[k]) Z_{(m,n),f}[k] \\ &=: A_2[k]d[k] + A_3[k]Z_{(m,n),f}[k]. \end{aligned} \tag{5}$$

Next, combine (4) and (5) in matrix form as

$$\begin{bmatrix} V_m[k] - V_n[k] + c[k] \\ V_m[k] \end{bmatrix} = \begin{bmatrix} A_1[k] & 0 \\ A_2[k] & A_3[k] \end{bmatrix} \begin{bmatrix} d[k] \\ Z_{(m,n),f}[k] \end{bmatrix}. \tag{6}$$

At each time t_k, the system of equations in (6) can be solved simultaneously to obtain estimates of the fault location and the fault-to-ground impedances. As we will show in Example 1, we can locate the unknown and possibly unsymmetric fault via the solution of (6). Note that the solvability of (6) can be ensured by checking that $A_1[k]$ and $A_3[k]$ are invertible. The matrix $A_1[k]$ is invertible as long as the entries of $Z^{\mathrm{s}}_{(m,n)}$ are nonzero, and the matrix $A_3[k]$ is invertible as long as the current in each phase of the transmission line is nonzero.

Example 1. We consider the canonical two-area test power system (see, e.g., [22]), with particular interest in one of the two identical 230-kV three-phase balanced transmission lines of length $220\,\mathrm{km}$ connecting the two area via buses m and n. A transposed distributed line model is used to simulate the transmission line. The PMUs are modelled in the MATLAB Simulink environment using the Fast Fourier Transform (FFT) function at the nominal 60-Hz frequency to obtain phasor magnitudes and phase angles. These values are reported once per electrical cycle, i.e., $\Delta t = 16.667\,\mathrm{ms}$. Then, via the method described in Section II-A, the abc-frame impedance matrix can be easily obtained using (3) as $Z_{(m,n)}$, in which the diagonal elements are $276.51\angle 62.931^\circ\,\Omega$ and the off-diagonal elements are $172.91\angle 48.669^\circ\,\Omega$.

Next, to illustrate the proposed fault location method summarized as (6), we choose simulation cases covering five types of faults: three phase to ground ($abcg$), double phase to ground (abg), single phase to ground (ag), three phase (abc), and double phase (ab). In each case, unbeknownst to operators, the fault occurs at a distance of $60\,\mathrm{km}$ from bus m with fault-to-ground resistance $5\,\Omega$ at time $t = 0\,\mathrm{s}$, and the fault sustains for three cycles before circuit breakers are tripped. Phasor measurements are collected at times $t_k = k\Delta t$, $k = 1, 2, 3$, i.e., at the end of each electrical cycle during the fault.

We first report and discuss results using measurements from the third cycle, i.e., in measurement window $2\Delta t < t \leq 3\Delta t$. The unknown variables $d[3]$ and $Z_{(m,n),f}[3]$ are solved via (6) and results are reported in Table I, based on which we make the following observations:

- *Fault location:* For all five fault types, the estimated distances are nearly identical to the actual location with errors of less than 0.1% normalized to the line length of $220\,\mathrm{km}$.
- *Faulted-phase identification:* For phases that remain intact, the estimated distances from bus m are unreasonably large, i.e., they are significantly greater than the line length. The corresponding fault-to-ground impedances have extremely large magnitudes, i.e., they represent open circuits. These observations are indicative of fault signature and help to identify the faulted phases.

On the other hand, Table II reports fault location and impedance estimates obtained with synchrophasor measurements from the first cycle, i.e., $0 < t \leq \Delta t$, of the during-fault period. By comparing Tables I and II, we find that the results from the former are much more accurate than those in the latter. Of particular concern is that errors in the estimated fault location grows from less than 0.1% to more than 2.0%, a sizeable increase. ■

TABLE I: (Example 1) Fault location and fault-impedance estimation using measurements from the *third* cycle of during-fault period.

Fault Type	$d^a[3]$		$d^b[3]$		$d^c[3]$		$Z^a_{(m,n),f}[3]$	$Z^b_{(m,n),f}[3]$	$Z^c_{(m,n),f}[3]$
	km	% Error	km	% Error	km	% Error			
$abcg$	60.060	0.027	60.080	0.036	60.007	0.003	$4.332\angle 3.607^\circ$	$5.183\angle 6.687^\circ$	$4.945\angle 0.470^\circ$
abg	59.978	0.010	59.995	0.002	2483.7	–	$5.683\angle -10.112^\circ$	$5.020\angle 33.005^\circ$	$1.803\times 10^7\angle -96.918^\circ$
ag	59.985	0.007	4044.4	–	1186.4	–	$4.921\angle 0.943^\circ$	$5.370\times 10^6\angle 54.002^\circ$	$1.010\times 10^7\angle -18.311^\circ$
abc	60.059	0.027	60.080	0.036	60.007	0.003	$4.332\angle 3.607^\circ$	$5.183\angle 6.688^\circ$	$4.945\angle 0.470^\circ$
ab	59.824	0.080	59.864	0.062	2414.4	–	$22.088\angle -11.559^\circ$	$19.038\angle 160.902^\circ$	$7.330\times 10^6\angle -159.306^\circ$

TABLE II: (Example 1) Fault location and fault-impedance estimation using measurements from the *first* cycle of during-fault period.

Fault Type	$d^a[1]$		$d^b[1]$		$d^c[1]$		$Z^a_{(m,n),f}[1]$	$Z^b_{(m,n),f}[1]$	$Z^c_{(m,n),f}[1]$
	km	% Error	km	% Error	km	% Error			
$abcg$	64.999	2.223	61.023	0.465	57.978	0.919	$30.766\angle 5.365^\circ$	$20.541\angle 34.746^\circ$	$46.341\angle 38.725^\circ$
abg	63.619	0.736	63.290	1.463	13425	–	$30.810\angle -6.595^\circ$	$21.816\angle 45.561^\circ$	$4.869\times 10^7\angle -145.285^\circ$
ag	62.997	1.362	15275	–	14420	–	$61.283\angle 10.380^\circ$	$1.354\times 10^8\angle 58.313^\circ$	$5.729\times 10^7\angle -60.366^\circ$
abc	64.998	2.272	61.023	0.465	57.978	0.919	$30.766\angle 5.365^\circ$	$20.541\angle 34.746^\circ$	$46.341\angle 38.725^\circ$
ab	63.875	1.761	63.932	1.787	2673.3	–	$38.005\angle -16.708^\circ$	$17.498\angle 88.404^\circ$	$7.616\times 10^6\angle -166.954^\circ$

C. Motivation for a Goodness-of-fit Metric

During faults or other fast transients, phasors extracted from PMUs may not accurately represent current/voltage waveforms as shown in Fig. 2a, where the current waveform reconstructed from phasor measurements is depicted by the dash-dot trace, while the original current signal is represented by the solid trace. We observe that the current waveform reconstructed from phasor measurements reasonably matches the actual signal in the third cycle during the fault, but not the first. Such discrepancies can lead to significant errors in applications that use these measurements, as we reveal in Example 1 with respect to fault location. Hence, the question arises as to how the fault-location application can assess the credibility of its results. As we show next, this problem can be tackled by appropriately evaluating the "goodness" of the fit between the signal that is reconstructed from the phasor measurements and the actual signal based on which the phasor was obtained. Such metrics quantify the accuracy of sychrophasors, which can in turn be related to the accuracy of fault-location results. In this way, these metrics can help indicate whether or not fault-location results obtained using particular synchrophasors are credible.

III. Goodness-of-fit Metric for Synchrophasor Measurements

Along a measurement window of length Δt, the PMU conducts FFTs on time-domain per-phase voltage and current waveforms and produces corresponding phasor representations with amplitude and phase components [9]. However, as highlighted in Section II-C, such phasor representations may not accurately reflect the time-domain waveforms if there are fast transients in the voltages and currents of interest. In such a case, the real-time application would benefit from additional quantities that describe the quality (i.e,. accuracy) of the synchrophasors. To this end, the so-called *goodness-of-fit* (GoF) metric evaluates the mismatch between the actual voltage or current waveform and the corresponding waveform reconstructed from their respective phasor measurements obtained from PMUs [16]. In this section, we define this metric (and a variant), highlight their key properties, demonstrate their usage via several numerical examples, and finally propose them as additional outputs to be provided by PMUs.

A. Definition of the GoF Metric

Denote the actual a-, b-, and c-phase voltage waveforms at bus m at time t by $\widehat{v}^a_m(t)$, $\widehat{v}^b_m(t)$, and $\widehat{v}^c_m(t)$, respectively. Similarly, let $\widehat{i}^a_{(m,n)}(t)$, $\widehat{i}^b_{(m,n)}(t)$, and $\widehat{i}^c_{(m,n)}(t)$ denote the actual currents in line (m,n). Within the measurement window $(k-1)\Delta t < t \le k\Delta t$ or simply k, a PMU at bus m samples the actual per-phase voltage and current waveforms at a rate of $N = 166$ samples-per-measurement-window (i.e., sampling time of $\Delta\tau = 100\,\mu$s) [17]. Then, the PMU conducts FFTs on the collected samples to produce corresponding phasor representations at time $t_k = k\Delta t$, which are sent to the application [23]. Denote the resultant a-, b-, and c-phase voltage phasors as $V^a_m[k] = |V^a_m[k]|\angle\phi^a_m[k]$, $V^b_m[k] = |V^b_m[k]|\angle\phi^b_m[k]$, and $V^c_m[k] = |V^c_m[k]|\angle\phi^c_m[k]$, respectively, with steady-state frequencies $\omega^a_m[k]$, $\omega^b_m[k]$, and $\omega^c_m[k]$, respectively. Further define $|V_m[k]| = [|V^a_m[k]|, |V^b_m[k]|, |V^c_m[k]|]^{\mathrm{T}}$, $\phi_m[k] = [\phi^a_m[k], \phi^b_m[k], \phi^c_m[k]]^{\mathrm{T}}$ and $\omega_m[k] = [\omega^a_m[k], \omega^b_m[k], \omega^c_m[k]]^{\mathrm{T}}$. Notation for measured phasor representations of per-phase current flows are established similarly.

With the above notation in place, we develop GoF-related concepts with respect to a-phase quantities, but note that b- and c-phase quantities would be evaluated analogously. Using the phasor magnitude, frequency, and phase information from a PMU, we can recover a corresponding reconstructed time-domain signal. For example, the reconstructed a-phase voltage and current waveforms are expressed as

$$v^a_m(t) = |V^a_m[k]| \cdot \cos(\omega^a_m[k]t + \phi^a_m[k]), \tag{7}$$

$$i^a_{(m,n)}(t) = |I^a_{(m,n)}[k]| \cdot \cos(\omega^a_m[k]t + \theta^a_{(m,n)}[k]), \tag{8}$$

where $(k-1)\Delta t < t \le k\Delta t$. The reconstructed signals in (7) and (8) differ from their corresponding actual waveforms by

$$\Delta v^a_m(t) = \widehat{v}^a_m(t) - v^a_m(t), \tag{9}$$

$$\Delta i^a_{(m,n)}(t) = \widehat{i}^a_{(m,n)}(t) - i^a_{(m,n)}(t). \tag{10}$$

Such discrepancies can be represented by the GoF as a single quantity over the measurement window k. As an example, the GoF metric (in [dB]) for the a-phase voltage and current are computed as [16]

$$\varphi^a_m[k] = 20\log\frac{|V^a_m[k]|}{\sqrt{\frac{1}{N-M}\sum_{j=1}^{N}\left(\Delta v^a_m(t_{k-1}+j\Delta\tau)\right)^2}}, \tag{11}$$

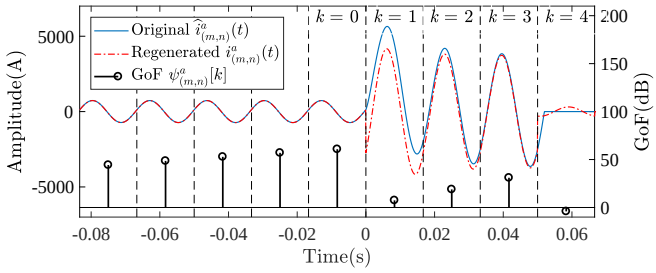

(a)

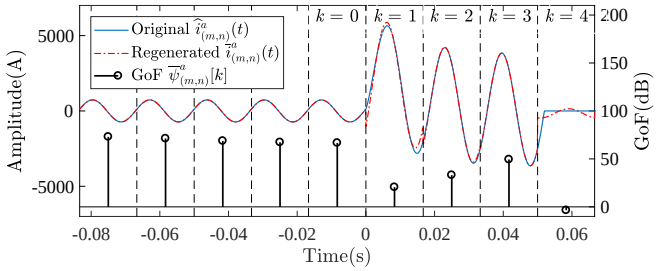

(b)

Fig. 2: (Examples 2 and 3) Phase-a actual current waveform and that reconstructed from PMU phasor measurements (a) without and (b) with DC-offset modification. Corresponding GoF values are superimposed. Fault initiates at the beginning of measurement window $k = 1$.

$$\psi^a_{(m,n)}[k] = 20\log \frac{|I^a_{(m,n)}[k]|}{\sqrt{\frac{1}{N-M}\sum_{j=1}^{N}\left(\Delta i^a_{(m,n)}(t_{k-1}+j\Delta\tau)\right)^2}}, \tag{12}$$

where N represents the number of samples in one measurement window (166 samples here) and M represents the number of estimated parameters to reconstruct the waveform. In our setting, $M = 3$, where the estimated parameters are amplitude, phase, and frequency. Finally, $\Delta\tau$ denotes the PMU internal sampling time in s. The GoF metric, as defined in (11) and (12), evaluates to a large value when the actual and reconstructed signals are well matched. The logarithmic function amplifies the range of GoF values in the case with greater mismatch between actual and reconstructed signals.

Next, via a numerical example, we illustrate how the GoF metric quantifies the mismatch between the PMU phasor measurement and the corresponding actual time-domain signal.

Example 2. Consider the transmission line of interest in Fig. 1b from Example 1. At $t = 0\,\text{s}$, we initiate a three-phase-to-ground fault with the fault resistance of $5\,\Omega$ on the line (m, n) (that is, $d^a = d^b = d^c = 60\,\text{km}$), which sustains for three cycles. Based on simulated actual waveforms and those reconstructed from PMU measurements, we evaluate GoFs in pre-fault, during-fault and post-fault operating conditions. Figure 2a contains the actual a-phase current waveform $\widehat{i}^a_{(m,n)}(t)$ (solid trace) and the corresponding one $i^a_{(m,n)}(t)$ reconstructed from phasor measurements (dash-dot trace). The GoF quantities are evaluated in each measurement window, which is marked by circles. Based on a visual examination of Fig. 2a, we make the following observations:

- *Pre-fault period ($k \le 0$):* The waveform reconstructed using PMU measurements matches the actual waveform obtained from simulations. In this period where the mismatch is minimal, evaluated GoFs $\psi^a_{(m,n)}[k] \approx 50\,\text{dB}$, $k \le 0$.
- *During-fault period ($1 \le k \le 3$):* Immediately following the fault initiation time $t = 0\,\text{s}$, the mismatch between the actual and reconstructed waveforms grows, so that the GoF evaluated in the first during-fault cycle is $\psi^a_{(m,n)}[1] = 7.5\,\text{dB}$. As the transients settle in measurement windows $k = 2, 3$, the match between the two waveforms improves, and the GoFs correspondingly increase to $\psi^a_{(m,n)}[k] = 19\,\text{dB}$ for $k = 2$, and $\psi^a_{(m,n)}[k] = 31\,\text{dB}$ for $k = 3$.
- *Post-fault period ($k > 3$):* After 3 cycles, i.e., at $t = 50$ ms, the fault is cleared by opening circuit breakers at both ends of the faulted line at near zero current. Following the disconnection of one line, the current through that line decreases sharply. Again, such a sudden change causes the mismatch between the waveforms to increase, and in turn leads to lower GoF in measurement window $k = 4$.

Here, we omit detailed discussion of voltage waveforms with respect to their mismatches and corresponding GoFs, but note that analogous analysis can be carried out. ■

B. Accounting for DC Offset

In Example 2, we observe that while there is nearly perfect match between the reconstructed and the actual waveforms in sinusoidal steady state, the mismatch is quite notable in the during-fault period, when the system experiences electrical transients. Recall that reconstructed signals (see, e.g., dash-dot trace in Fig. 2a) are recovered from the amplitude, phase, and frequency values, which are obtained via the PMU, using (7) and (8). However, the three aforementioned parameters do not encode information about the DC offset of the actual waveform, which may be nonzero during electrical transients. As a result, the GoF metric may be decrease in value simply due to a DC offset, and not errors in the phasor information reported. For example, this intuition is evident via visual inspection of Fig. 2a for $k = 1$. Thus, we devote some time to investigate the effects of such DC offsets on the GoF metric.

The DC offset can be easily computed by the PMU at time t_k for the previous measurement window $(k-1)\Delta t < t \le k\Delta t$. As an example, DC offsets for a-phase voltage and current are evaluated as:

$$\Delta\overline{v}^a_m[k] = \frac{1}{N}\sum_{j=1}^{N}\Delta v^a_m(t_{k-1}+j\Delta\tau), \tag{13}$$

$$\Delta\overline{i}^a_{(m,n)}[k] = \frac{1}{N}\sum_{j=1}^{N}\Delta i^a_{(m,n)}(t_{k-1}+j\Delta\tau), \tag{14}$$

respectively. These can be interpreted as the mean value of the difference between the actual and reconstructed signals in measurement window k. Now, using the DC-offset information in conjunction with PMU phasor measurements (i.e., amplitude, phase, and frequency), we hope that the reconstructed waveforms would more closely match the actual ones. For

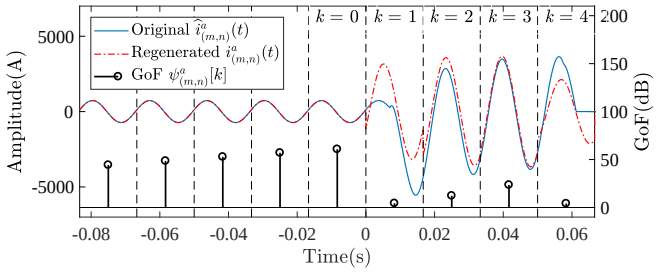

(a)

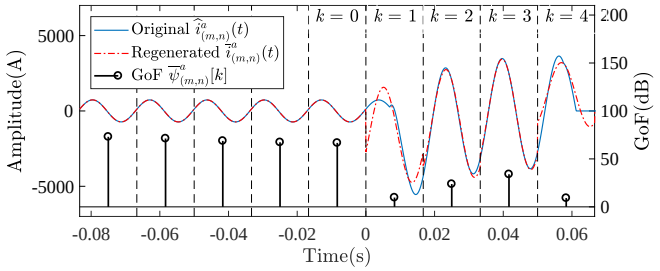

(b)

Fig. 3: (Example 4) Phase-a actual current waveform and that reconstructed from PMU phasor measurements (a) without and (b) with DC-offset modification. Corresponding GoF values are superimposed. Fault initiates at $t = 6.94\,\text{ms}$, within measurement window $k = 1$.

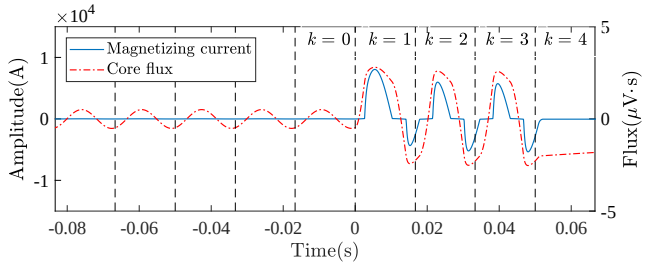

(a)

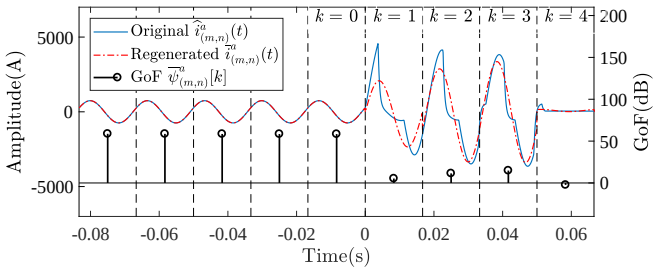

(b)

Fig. 4: (Example 5) Current transformer (CT) flux saturation limit is set to $2\,\mu$V·s. (a) Phase-a CT magnetizing current and core flux. (b) Phase-a actual current waveform and that reconstructed from PMU phasor measurements with DC-offset modification. Fault initiates at the beginning of measurement window $k = 1$.

example, for $(k-1)\Delta t < t \leq k\Delta t$, the reconstructed a-phase voltage and current waveforms can be expressed as

$$\overline{v}^a_m(t) = v^a_m(t) + \Delta\overline{v}^a_m[k] \tag{15}$$

$$\overline{i}^a_{(m,n)}(t) = i^a_{(m,n)}(t) + \Delta\overline{i}^a_{(m,n)}[k], \tag{16}$$

respectively, where $v^a_m(t)$ and $i^a_{(m,n)}(t)$ are obtained from (7) and (8), respectively. Accordingly, the mismatch between the actual waveforms and the ones reconstructed from synchrophasors (accounting for DC offset) are computed as $\widehat{v}^a_m(t) - \overline{v}^a_m(t)$ and $\widehat{i}^a_{(m,n)}(t) - \overline{i}^a_{(m,n)}(t)$. Finally, these can be substituted into (11) and (12) to obtain updated GoF metrics $\overline{\varphi}^a_m[k]$ and $\overline{\psi}^a_{(m,n)}[k]$ for the a-phase voltage and current, respectively.

Example 3 (Effect of DC Offset on GoF Metrics)**.** Consider the same system and fault scenario as in Example 2, but in addition to $|I^a_{(m,n)}[k]|$, $\theta^a_{(m,n)}[k]$, and $\omega^a_m[k]$, assume that the DC offset obtained from (14) is available. The reconstructed current waveform is superimposed onto the actual one in Fig. 2b. In this case, in contrast to Fig. 2a, the reconstructed and actual waveforms match much more closely, with the greatest improvement in the during-fault period, especially in measurement window $k = 1$. Correspondingly, as compared with Example 2, GoF values are greater in the during-fault period, as depicted in Fig. 2b. Specifically, in the problematic measurement window $k = 1$ from Example 2, the GoF increases from $7.5\,\text{dB}$ to $20.5\,\text{dB}$. ■

Previously, by making available the DC offset of the actual signal obtained from (13) and (14), we significantly improve the match between the actual waveform and that reconstructed from PMU measurements, as illustrated in Example 3. On the other hand, as we show next via Examples 4 and 5, respectively, the problem of matching the reconstructed waveform to the actual one is further complicated if (i) the fault initiation time does not coincide with the measurement window boundary, or (ii) the current transformer (CT) saturates due to large line currents.

Example 4 (Effect of Fault Initiation Time on GoF Metrics)**.** In the scenario used in Examples 2 and 3, the fault initiation time fortuitously coincides with the boundary between two consecutive measurement windows. In this example, we consider the same system and fault scenario as before, except the fault initiation time is set to $t = 6.94\,\text{ms}$, which is close to the centre of the measurement window $k = 1$, as shown in Fig. 3. Evident from a visual inspection of Fig. 3a, in which the reconstructed waveform is obtained using only current phasor estimates, the substantial mismatch in measurement window $k = 1$ cannot be completely obviated by a simple DC offset. This observation is substantiated in Fig. 3b, where the reconstructed waveform incorporates the DC offset in the actual signal. Specifically, in measurement window $k = 1$, the GoF with the DC-offset modification is $9.7\,\text{dB}$ as compared to $4.4\,\text{dB}$ in Fig. 3a. Indeed, while the improvement in the match is less significant than that observed in Example 3, by considering the DC offset, the mismatch is still reduced. ■

Example 5 (Effect of Current-transformer Saturation on GoF Metrics)**.** The measurement accuracy of monitoring and protection devices such as PMUs and relays depends on the quality of analog signals obtained from CTs [24]. Examples 2–

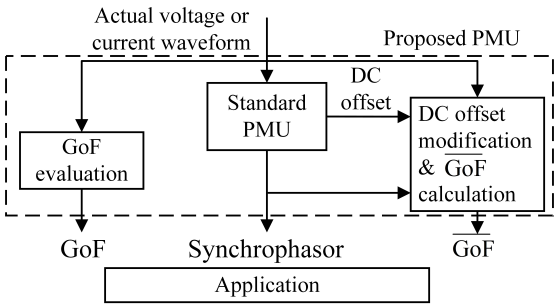

Fig. 5: Schematic of proposed PMU.

4 assumed an ideal CT model without saturation. In reality, due to the nonlinear characteristic of its core, the CT is vulnerable to the saturation phenomenon when line-current magnitudes are much higher than their steady-state values [25]. In this example, we consider the same scenario as in Examples 2 and 3, except a non-ideal CT model is used and the core flux saturation limit is set to $2\,\mu$V·s. As shown in Fig. 4a, following the increase of the core flux to an amplitude more than $2\,\mu$V·s, the CT saturates and the magnetizing current increases sharply. Then, as shown in Fig. 4b, the saturation phenomenon leads to non-sinusoidal current waveforms (as seen by the PMU) in the during-fault period. Again, we note that the mismatch between the original and the reconstructed waveforms cannot be removed by a simple DC offset. ■

Via Examples 3–5, we observe that the GoF metric quantifies the error of the reported synchrophasor, and GoF values may be improved when the reconstructed signal considers the mean DC offset in a measurement window $(k-1)\Delta t < t \leq k\Delta t$. Thus, we hypothesize that GoF metrics can serve as a predictor for the performance quality of real-time applications, such as fault location.

C. Inclusion of GoF Metrics in the PMU

Base on the discussion above, we propose to include the GoF and its DC-offset-modified variant as prescribed quantities for the PMU to transmit to real-time applications. In the proposed structure (marked as the dashed trace in Fig. 5), in addition to the phasor information (amplitude, phase, and frequency) reported by the standard PMU, the GoF and $\overline{\text{GoF}}$ (which denotes the GoF-variant that quantifies the mismatch between the original signal and the one reconstructed accounting for DC offset) are also computed and transmitted. It is worth noting that we do *not* advocate to transmit the DC offset itself to the application, because our goal is not to reconstruct the actual voltage and current waveforms at the application, but rather to determine whether or not real-time application results are credible. Next, via numerical case studies, we illustrate how the GoF metrics can help to predict the performance quality of the fault-location application.

IV. Case Studies

In this section, we demonstrate the advantage of incorporating GoF metrics into PMUs by applying them to the fault-location application. In Example 1, we considered five fault

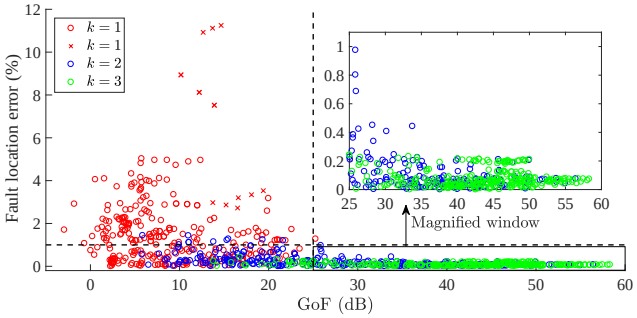

(a)

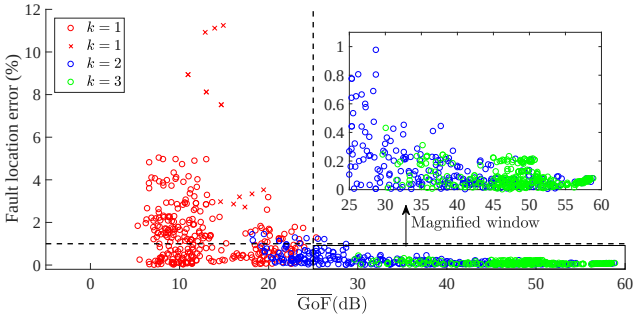

(b)

Fig. 6: Fault location error versus GoF values computed for waveforms reconstructed from PMU phasor measurements obtained in measurement windows $k = 1, 2, 3$ (a) without and (b) with DC-offset modification. The $\times$ markers denote cases in which fault initiates $12.5\,\text{ms}$ (equivalent to $3/4$ of the measurement window length) into measurement window $k = 1$.

types: $abcg$, abg, ag, abc, and ab. Here, in order to include all fault conditions in our simulations, we also consider variations in (i) fault resistance, (ii) fault location along the line, and (iii) fault initiation time with respect to measurement window boundaries. Particularly, for each fault type, simulations cover fault resistances of $5\,\Omega$, $20\,\Omega$, and $30\,\Omega$, fault locations of 10, 60, 110, 160, and $210\,\text{km}$ from bus m, and 4 fault initiation times equally spaced within a measurement window. Thus, in total, we conduct 60 simulations for each of the five fault types. In each simulation, we assume that the fault lasts for three electrical cycles, which provides three synchrophasors for the during-fault period. Each set of synchrophasors (corresponding to a "case") is used to locate the fault and estimate the fault-to-ground impedance via (6).

A. Simulation Results

For each case, we obtain synchrophasor measurements of $I_{(m,n)}$ and $I_{(n,m)}$ at buses m and n, respectively, as well as their corresponding GoF values. Then, for each pair of current measurements obtained at either end of the line, we take the average of the two GoF values. As shown in Fig. 6a, we subsequently plot the fault location error in each case against the average GoF of corresponding measurements. Fault location results obtained using synchrophasors from measurement windows $k = 1, 2, 3$ of the during-fault period are marked in red, blue, and green colours, respectively. Via visual inspection of Fig. 6a, we observe that the greater fault location errors ($> 1\%$) are predominantly associated with

TABLE III: (Remark 1) Comparison of fault-location accuracy with corresponding GOF metrics for an $abcg$ fault occurring at $60\,\mathrm{km}$ from bus m with $R_g = 5\,\Omega$. Fault initiates at the beginning of measurement window $k = 1$.

	Measurement window $k = 1$			Measurement window $k = 3$		
	% Error	GoF	$\overline{\text{GoF}}$	% Error	GoF	$\overline{\text{GoF}}$
Without saturation	0.6463	6.6909	19.239	0.1375	32.978	45.808
With saturation	21.628	4.0000	4.1050	1.9305	17.990	18.195

synchrophasors obtained measurement window $k = 1$, with low GoF values ($< 25\,\mathrm{dB}$). Here, thresholds of 1% and $25\,\mathrm{dB}$ are considered to facilitate subsequent discussions, but they may be tailored for each application scenario based on the user's tolerance for accuracy. Moreover, it is worth noting that within each fault type considered, cases in which the fault initiates $12.5\,\mathrm{ms}$ (equivalent to $3/4$ of the measurement window length) into measurement window $k = 1$ are associated with the highest fault-location errors (marked as red $\times$'s in Fig. 6a). In these, the PMU does not have enough information from the during-fault period, so the resulting phasor leads to a poor fit between the time-domain waveform and that reconstructed from the phasor, as previously highlighted in Fig. 3a. On the other hand, synchrophasors obtained in measurement window $k = 3$ (and some from $k = 2$) are associated with higher GoF values (greater than $25\,\mathrm{dB}$), which indicate good fit. Corresponding fault-location errors are less than 1%. These results echo the phenomenon observed in Example 1 for fault-to-ground impedance of $5\,\Omega$ and fault location of $60\,\mathrm{km}$ from bus m.

Recall from Example 3 that a simple constant DC-offset modification can significantly improve the GoF value for the reconstructed waveform. Thus, we also compute the GoF values after DC-offset modification (we call this GoF variant $\overline{\text{GoF}}$). Similar to Fig. 6a, we plot fault location error for each case against its corresponding $\overline{\text{GoF}}$ value in Fig. 6b. Using this modified GoF metric, many of the cases with acceptable fault location errors (less than 1%) are shifted to the right with $\overline{\text{GoF}}$ values greater than $25\,\mathrm{dB}$. Particularly, in Fig. 6a, there are 445 cases with GoF values greater than $25\,\mathrm{dB}$, all of which correspond to sufficiently accurate fault location errors of less than 1%. On the other hand, in Fig. 6b, 89 more cases with sufficiently accurate fault location results are identified based on the criterion that their corresponding $\overline{\text{GoF}}$ values are greater than $25\,\mathrm{dB}$. Thus, we conclude that indeed, the modified GoF metric is able to better distinguish cases whose fault location results are sufficiently accurate.

Remark 1 (Effect of Current-transformer Saturation)**.** Table III reports fault location accuracy using synchrophasors obtained in measurement windows $k = 1$ and $k = 3$, as well as their corresponding GoF and $\overline{\text{GoF}}$ values. Comparing the rows in Table III, we observe that GoF and $\overline{\text{GoF}}$ values are similarly low when CT saturation occurs. This is because the mismatch between the original and reconstructed waveforms is not due to DC offset, as noted in Example 5. Even though GoF and $\overline{\text{GoF}}$ values are similar, their low values still provide a good predictor for uncredible fault-location results. Particularly, in both measurement windows $k = 1$ and $k = 3$, fault-location errors are quite high, which are reflected in low GoF and $\overline{\text{GoF}}$ values. In fact, the closeness of the two values indicates that the reason for low GoF is not DC offset, but that the waveform is actually distorted. ■

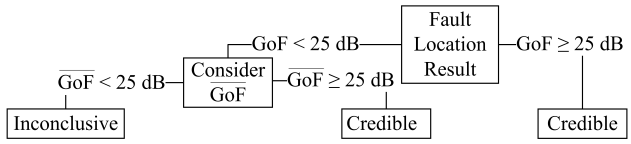

Fig. 7: Proposed decision tree to assess credibility of fault location.

B. GoF Criteria for Predicting Fault Location Accuracy

After a fault occurs, as shown in Fig. 5, synchrophasor measurements and corresponding GoF or $\overline{\text{GoF}}$ values are received by the fault-location application, which utilizes (i) the synchrophasors to determine the location of the fault, and (ii) the GoF or $\overline{\text{GoF}}$ values to assess whether or not the fault-location results are sufficiently credible. Based on the discussion in Section IV-A, we note that a GoF value of $25\,\mathrm{dB}$ is a reasonable demarcation in this case to determine whether or not fault location results are sufficiently credible.

Using the decision process outlined in Fig. 7, we first consider cases with GoF $> 25\,\mathrm{dB}$ and conclude that, as shown in Fig. 8a, they predominantly correspond to fault location errors of less than 0.5%, and 73.03% of those cases correspond to errors of less than 0.1%. If $\overline{\text{GoF}}$ is not available because the PMU is not equipped to obtain the DC offset of time-domain measurement waveforms, the assessment would end here. However, in the case that $\overline{\text{GoF}}$ is available to the application, we note that nearly all the cases with GoF $< 25\,\mathrm{dB}$ but $\overline{\text{GoF}} > 25\,\mathrm{dB}$ correspond to fault location errors of less than 1% as shown in Fig. 8b, and 86.52% of the cases have errors of less than 0.5%. Finally, as shown in Fig. 8c, cases with GoF $< 25\,\mathrm{dB}$ and $\overline{\text{GoF}} < 25\,\mathrm{dB}$ have fault location errors in a wide range (as high as nearly 12%). By observing Fig. 8, we conclude that cases with GoF $> 25\,\mathrm{dB}$ or those with $\overline{\text{GoF}} > 25\,\mathrm{dB}$ return credible fault-location results, but cases with GoF $< 25\,\mathrm{dB}$ or $\overline{\text{GoF}} < 25\,\mathrm{dB}$ are inconclusive.

V. Concluding Remarks and Directions for Future Research

This paper illustrates the usability of GoF metrics to quantify synchrophasor accuracy in real-time applications. Specifically, for fault location along a transmission line, GoF metrics indeed yield an assessment for the confidence level of fault-location results. Thus, we advocate that the PMU transmits GoF values in addition to the standard synchrophasor output to various real-time applications. Additionally, based on aggregate results from extensive case studies, we provide GoF criteria under which fault-location results can be deemed to be sufficiently credible. A particularly relevant extension of this work is to develop PMU models that incorporate DC offsets in the measured signals and GoF metrics as outputs. Other compelling directions for future work include investigating the role of GoF metrics in other real-time applications, such as special protection schemes, transient stability assessment, and dynamic state estimation.

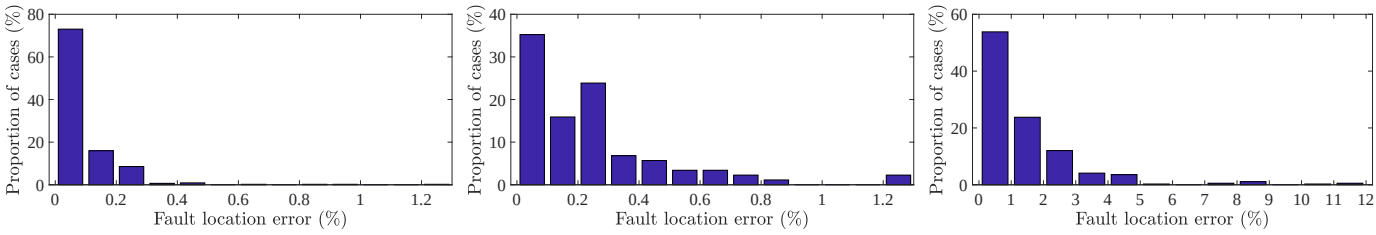

Fig. 8: Proportion of cases corresponding to particular ranges of fault location errors out of a total of (a) 445 cases with GoF $> 25\,\mathrm{dB}$, (b) 89 cases with GoF $< 25\,\mathrm{dB}$ and $\overline{\mathrm{GoF}} > 25\,\mathrm{dB}$, and (c) 366 cases with GoF $< 25\,\mathrm{dB}$ and $\overline{\mathrm{GoF}} < 25\,\mathrm{dB}$.

REFERENCES

[1] M. M. Saha, J. J. Izykowski, and E. Rosolowski, *Fault location on power networks*. Springer Science & Business Media, 2009.

[2] T. Takagi, Y. Yamakoshi, M. Yamaura, R. Kondow, and T. Matsushima, "Development of a new type fault locator using the one-terminal voltage and current data," *IEEE Transactions on Power apparatus and systems*, no. 8, pp. 2892–2898, Aug. 1982.

[3] C. E. de Morais Pereira and L. C. Zanetta, "Fault location in transmission lines using one-terminal postfault voltage data," *IEEE Transactions on Power Delivery*, vol. 19, no. 2, pp. 570–575, Mar. 2004.

[4] A. T. Johns and S. Jamali, "Accurate fault location technique for power transmission lines," *IEE Proceedings C - Generation, Transmission and Distribution*, vol. 137, no. 6, pp. 395–402, Nov. 1990.

[5] J. Izykowski, E. Rosolowski, M. M. Saha, M. Fulczyk, and P. Balcerek, "A fault-location method for application with current differential relays of three-terminal lines," *IEEE Transactions on Power Delivery*, vol. 22, no. 4, pp. 2099–2107, Oct. 2007.

[6] D. Novosel, D. G. Hart, E. Udren, and J. Garitty, "Unsynchronized two-terminal fault location estimation," *IEEE Transactions on Power Delivery*, vol. 11, no. 1, pp. 130–138, Jan. 1996.

[7] J. Izykowski, E. Rosolowski, P. Balcerek, M. Fulczyk, and M. M. Saha, "Accurate noniterative fault-location algorithm utilizing two-end unsynchronized measurements," *IEEE Transactions on Power Delivery*, vol. 26, no. 2, pp. 547–555, Apr. 2011.

[8] D. Novosel, V. Madani, B. Bhargave, K. Vu, and J. Cole, "Dawn of the grid synchronization," *IEEE Power and Energy Magazine*, vol. 6, no. 1, pp. 49–60, Jan. 2008.

[9] "IEEE Standard for Synchrophasor Measurements for Power Systems," *IEEE Std C37.118.1-2011 (Revision of IEEE Std C37.118-2005)*, Dec. 2011.

[10] "IEEE Standard for Synchrophasor Data Transfer for Power Systems," *IEEE Std C37.118.2-2011 (Revision of IEEE Std C37.118-2005)*, Dec. 2011.

[11] M. Kezunovic, S. Meliopoulos, V. Venkatasubramanian, and V. Vittal, *Application of Time-synchronized Measurements in Power System Transmission Networks*. Springer, 2014.

[12] A. S. Dobakhshari, "Noniterative parameter-free fault location on untransposed single-circuit transmission lines," *IEEE Transactions on Power Delivery*, vol. 32, no. 3, pp. 1636–1644, Jun. 2017.

[13] M. Kezunovic, "Smart fault location for smart grids," *IEEE Transactions on Smart Grid*, vol. 2, no. 1, pp. 11–22, Mar. 2011.

[14] G. Feng and A. Abur, "Fault location using wide-area measurements and sparse estimation," *IEEE Transactions on Power Systems*, vol. 31, no. 4, pp. 2938–2945, Jul. 2016.

[15] "IEEE Standard for Synchrophasor Measurements for Power Systems – Amendment 1: Modification of Selected Performance Requirements," *IEEE Std C37.118.1a-2014 (Amendment to IEEE Std C37.118.1-2011)*, Apr. 2014.

[16] A. Riepnieks and H. Kirkham, "An introduction to goodness of fit for PMU parameter estimation," *IEEE Transactions on Power Delivery*, vol. 32, no. 5, pp. 2238–2245, Oct. 2017.

[17] A. J. Roscoe, I. F. Abdulhadi, and G. M. Burt, "P and M class phasor measurement unit algorithms using adaptive cascaded filters," *IEEE Transactions on Power Delivery*, vol. 28, no. 3, pp. 1447–1459, Jul. 2013.

[18] P. Castello, J. Liu, C. Muscas, P. A. Pegoraro, F. Ponci, and A. Monti, "A fast and accurate PMU algorithm for P + M class measurement of synchrophasor and frequency," *IEEE Transactions on Instrumentation and Measurement*, vol. 63, no. 12, pp. 2837–2845, Jun. 2014.

[19] D. R. Gurusinghe, A. D. Rajapakse, and D. Muthumuni, "Modeling of a synchrophasor measurement unit in an electromagnetic transient simulation program," in *Proc. Int. Conf. on Power System Transients*, 2012.

[20] I. Ivanov and A. Murzin, "Synchrophasor-based transmission line parameter estimation algorithm taking into account measurement errors," in *2016 IEEE PES Innovative Smart Grid Technologies Conference Europe*, Oct. 2016.

[21] J. J. Grainger and W. D. Stevenson, *Power system analysis*. McGraw-Hill, 1994.

[22] P. Kundur, N. J. Balu, and M. G. Lauby, *Power system stability and control*. McGraw-hill New York, 1994.

[23] H. Kirkham and A. Riepnieks, "Dealing with non-stationary signals: Definitions, considerations and practical implications," in *Proc. Power and Energy Society General Meeting*, 2016.

[24] B. M. Schettino, C. A. Duque, P. M. Silveira, P. F. Ribeiro, and A. S. Cerqueira, "A new method of current-transformer saturation detection in the presence of noise," *IEEE Transactions on Power Delivery*, vol. 29, no. 4, pp. 1760–1767, Aug. 2014.

[25] E. Hajipour, M. Vakilian, and M. Sanaye-Pasand, "Current-transformer saturation prevention using a controlled voltage-source compensator," *IEEE Transactions on Power Delivery*, vol. 32, no. 2, pp. 1039–1048, Apr. 2017.